International Journal of Pure and Applied Chemistry
ijpac.eanso.org
Volume 3, Issue1, 2025
Print ISSN: 2790-9565 | Online ISSN: 2790-9573
Title DOI: https://doi.org/10.37284/2790-9573

EAST AFRICAN
NATURE &
SCIENCE
ORGANIZATION

Original Article

Electrochemical Reduction of Carbon Dioxide to Formate by Tin-based Metal-Organic Frameworks

Dr. Austin Chipojola Mtukula[1*], *Prof. Wen-Chuan Lai, PhD*[2] & & *Prof. Zhi-Yuan Gu, PhD*[3]

[1] Nalikule College of Education, P. O. Box 40680, Kanengo, Lilongwe, Malawi.
[2] Jiangsu Collaborative Innovation Center of Biomedical Functional Materials, Nanjing, China.
[3] Nanjing Normal University, Nanjing 210023, China.
[*] Author for Correspondence Email: austin.mtukula@yahoo.com

Article DOI: https://doi.org/10.37284/ijpac.3.1.2738

Date Published:

02 March 2025

Keywords:

Metal-Organic Frameworks (MOFs), Electrochemical Carbon Dioxide Reduction Reaction (eCO2RR), Formate, Hydrothermal Synthesis Method, Selectivity.

ABSTRACT

There is an urgent need to develop new technologies for converting greenhouse gas CO2 into useful products to address environmental and energy crises simultaneously. Electrochemical CO2 reduction reaction (eCO2RR) driven by renewable electricity affords a capable route to realizing a carbon-neutral future and combating a global climate predicament. In determining the relationship between synthesis approach, catalyst structure and performance, two Sn-MOF electrocatalysts were produced with a bottom-up hydrothermal method. A two-dimensional catalyst 2D Sn-BDC was prepared by the open hydrothermal synthesis method, while a three-dimensional catalyst 3D Sn-BDC was prepared under the closed hydrothermal method. In CO2-saturated 0.5 M KHCO3 aqueous solution, 2D Sn-BDC catalyst displayed good performance compared with 3D Sn-BDC catalyst for CO2 reduction to formate with Faradaic efficiency of 96.3 %, partial current density of 10.0 mA cm-2 at an overpotential of 0.42 V, TOF of 4887 h-1, charge transfer resistance of 42.98 Ω and over a 10 h stability. It is recognized that the superiority of 2D Sn-BDC is assumed to originate from the ultrathin structure, enhanced surface area and presence of surface vacancies. Consequently, the improvement in mass transport, accessibility of Sn active sites and carrier concentration resulted in high catalytic performance.

APA CITATION

Mtukula, A. C., Lai, W. & Gu, Z. (2025). Electrochemical Reduction of Carbon Dioxide to Formate by Tin-based Metal-Organic Frameworks. *International Journal of Pure and Applied Chemistry*, *3*(1), 1-14. https://doi.org/10.37284/ijpac.3.1.2738.

CHICAGO CITATION

Mtukula, Austin Chipojola, Wen-Chuan Lai and Zhi-Yuan Gu. 2025. “Electrochemical Reduction of Carbon Dioxide to Formate by Tin-based Metal-Organic Frameworks”. *International Journal of Pure and Applied Chemistry 3* (1), 1-14. https://doi.org/10.37284/ijpac.3.1.2738.

HARVARD CITATION

Mtukula, A. C., Lai, W. & Gu, Z. (2025) “Electrochemical Reduction of Carbon Dioxide to Formate by Tin-based Metal-Organic Frameworks”, *International Journal of Pure and Applied Chemistry*, 3(1), pp. 1-14. doi: 10.37284/ijpac.2.1.2738.

IEEE CITATION

A. C. Mtukula, W. Lai & Z. Gu. “Electrochemical Reduction of Carbon Dioxide to Formate by Tin-based Metal-Organic Frameworks”, IJPAC, vol. 1, no. 3, pp. 1-14, Mar. 2025.

MLA CITATION

Mtukula, Austin Chipojola, Wen-Chuan Lai & Zhi-Yuan Gu. “Electrochemical Reduction of Carbon Dioxide to Formate by Tin-based Metal-Organic Frameworks”. *International Journal of Pure and Applied Chemistry*, Vol. 3, no. 1, Mar. 2025, pp. 1-14, doi:10.37284/ijpac.3.1.2738.

INTRODUCTION

The reduction of carbon dioxide (CO_2) to fuels and feed stalks is an imperative factor of an imminent energy conservation approach to alleviate carbon levels and its associated challenges. The CO_2 conversion into desirable products can combat both CO_2 emission and fossil fuel dependence [1, 2, 3, 4-5]. Formate ($HCOO^-$) a raw material and a fuel, is among the products of CO_2 conversion [6]. Due to environmental friendliness, p-block metal-based catalysts are among the currently studied catalysts for formic acid production with reported good performances [7, 8]. The electrochemical reduction of carbon dioxide (eCO_2RR) has attracted significant research attention, nevertheless, selectivity, low charge transfer and stability are among the limiting factors to be improved for large-scale applications. The challenges are mostly due to high energy barrier, slow kinetics, mixed products and the presence of impurities in the eCO_2RR[9, 10-11]. Therefore, for large-scale applications, promising eCO_2RR electrocatalysts should possess a low overpotential, a high current density, and good stability, while in the process suppressing any side reaction to obtain specific products. Consequently, it is significant to design an appropriate eCO_2RR electrocatalyst to realize satisfactory activity and selectivity of $HCOO^-$ production.

Metal-organic frameworks (MOFs) have enticed research devotion for application in eCO_2RR due to exceptional properties such as ordered porous structures, large surface area and modifiable structure which are vital factors in improving chemical activity [12-18]. It is thought that the polyaromatic carboxylic acids create several coordination sites that assist in synthesizing MOFs of different structures in addition to firm conformation and the presence of carboxylate groups that lead to strong coordination ability [19-22]. It is noted that the strength of MOF structure is totally dependent on the nature of the metal, ligand and the associated bond [23]. Hence, the structural features of the MOFs are based on the net topology which is highly dependent on the connectivity and symmetry of the metal nodes and ligands [20, 24]. It is well-known that the attainment of the structure and net topology is highly influenced by the nature of the metal node, ligand, reagents, stoichiometry and temperature, besides the synthesis methods which can alter and elevate the properties of the MOF catalysts [25-31]. Thus, the understanding of the intrinsic properties of MOF’s nodes and ligands may influence design approaches that can maximize the synergetic interactions and activity of a catalyst in addition to electrolyte, metal loading/sizes and potential effect on performance [32-34]. However, proper catalyst design and synthesis method are crucial to optimize catalyst composition, morphology, performance and stability. Sn-based catalysts have been studied in eCO_2RR and established good selectivity for the production of formate; as oxide, alloys and non-metallic doped catalysts [35-41]. Furthermore, some Sn-MOFs have been studied as precursors rather than directly being used in catalysis [42]. However, it has been realized that the use of pristine MOFs may reduce both energy usage and cost for the decomposition of the organic linkers and also prevent an unavoidable collapse of the reticular structure [43].

In view of the exceptional properties of Sn nodes and organic ligands: 1, 4-benzene dicarboxylic acid (BDC), we effectively synthesized a 2D Sn-BDC catalyst through an open hydrothermal synthesis stirring approach. The as-synthesized 2D Sn-BDC catalyst has a framework of para-phthalic acid (BDC) as a linker with Sn nodes bound to O atoms [44], **Figure 1a-b**. In determining the relationship between synthesis approach, topology and electrocatalytic performance; a 3D Sn-BDC catalyst was synthesized through a closed hydrothermal synthesis method. Overall, this work has recognized that the open hydrothermal synthesis stirring approach created a two-dimensional framework, 2D Sn-BDC with improved formate efficiency and suppression of hydrogen and CO evolution. Although Sn-MOFs was used as eCO_2RR catalyst in a recent publication [45], the difference of our approach is the use of p-phthalic acid (1, 4-BDC) as a ligand for Sn nodes, use of pristine 2D Sn-BDC in eCO_2RR, use of two synthesis methods (closed and open hydrothermal synthesis methods) and the catalytic performance of 2D Sn-BDC is much improved with FE_{HCOO^-} = 96.3% at an overpotential (η) = 0.42. In our present work, a significant difference in eCO_2RR performance exists among 2D Sn-BDC, 3D Sn-BDC and SnO_2, due to variations in structures, morphology and number of active sites. To the best of our knowledge, this work might imply that pristine 2D Sn-BDC could be among the prominent tin polyaromatic-based MOF catalyst for reduction of carbon dioxide into formate with high efficiency, high current density at low overpotential.

EXPERIMENTAL SECTION

All experiments used chemicals of analytical grade without any purification.

Synthesis of 2D Sn-BDC MOF

2D Sn-BDC MOF was synthesized by a bottom-up open hydrothermal stirring process[45]. Solution 1 was prepared by using 0.96g of NaOH and 1.99g of p-phthalic acid premixed in 200 mL of distilled water. Solution 2 was set by dissolving 2.71g of $SnCl_2·2H_2O$ in 40 mL of distilled water. Then, Solution 2 was slowly added to Solution 1 by stirring in a water bath. Consequently, the solution mixture was further stirred for 1h in the water bath at 90 ºC, followed by constant stirring at 60 ºC for another 10h. Lastly, the acquired white precipitates were washed many times with DMF and ethanol and dried at 80°C[44].

Synthesis of 3D Sn-BDC MOF

Through a bottom-up closed hydrothermal synthesis approach [31], 3D Sn-BDC MOF was prepared by mixing $LiOH.H_2O$ (82mg), p-phthalic (1, 4-BDC) acid (498 mg), $SnSO_4$ (165mg) and H_2O (3 mL). The mixture was later sealed in a Teflon vessel (23 mL inner volume) in air and heated at 160 ^{o}C for 72 h. The yielded crystals were washed with N, N-dimethylformamide (DMF), and methanol then dried at 80 ^{o}C.

Preparation of Working Electrode

A homogeneous catalyst ink for each sample was prepared from a mixture of 10.0 mg catalyst powder, 2.0 mg carbon powder, 1000μL of ethanol and 100 μL of Nafion D-521 (5 wt %) via ultrasonication [4]. Later, 1000 μL catalyst ink was loaded onto 10 pieces of 1×1 cm^2 carbon paper. The loaded carbon papers were finally dried in an oven at 100 ^{0}C.

Characterization

Powder X-ray diffraction (PXRD) patterns of the materials were obtained using a Rigaku 9 kW Instruments (Japan) D/MAX-2500 diffractometer with Cu Kα radiation (λ=1.54056 Å). The morphology of the materials was characterized using scanning electron microscopy (SEM, JSM-7600, JEOL Ltd, Japan) and X-ray photoelectron spectroscopy (XPS). Fourier transform infrared spectroscopy (FTIR) spectra were obtained using an ALPHA II (Bruker) instrument. Energy Dispersive Spectroscopy (EDS) measurements were recorded with a JEOL 7500F Field Emission scanning electron microscope. Electron paramagnetic resonance (EPR), was employed to detect oxygen vacancies associated with either missing BDC linker defects or unsaturated Sn metal defects [45].

Electrochemical Measurements

Gas products were quantitatively analyzed using a gas chromatograph (PANNA A91). Formate content was obtained for quantitative analysis using a high-performance liquid chromatograph (Waters 501). All electrochemical data were acquired using Shanghai Chenhua CHI660E. The electrochemical measurements were conducted in an H-cell joined with an electrochemical workstation. The H-type cell comprised of working electrode = (catalyst electrode), (Ag/AgCl electrode, saturated KCl) = reference electrode, (Pt plate) electrode = counter electrode and a 0.5 M $KHCO_3$ solution[4, 45]. The level of CO_2 in the $KHCO_3$ electrolyte was maintained by a continuous supply of CO_2 throughout the experiments. Cyclic voltammetry (CV) analysis was carried out to determine catalyst activities and matching potentials. Afterwards, faradaic efficiencies (FE) for the reduction products and turn-over frequencies (TOF) were calculated[4]. Electrochemical impedance spectroscopy (EIS) was used to scrutinize the activity of catalyst electrodes by using the three-electrode H-Type cell in 0.5 M $KHCO_3$ solution.

RESULTS AND DISCUSSION

Catalyst Characterization

Firstly, powder X-ray diffraction (PXRD) and scanning electron microscopy (SEM) were used in the morphology characterization of the as-prepared 2D Sn-BDC and 3D Sn-BDC electrocatalysts. In all the tests, the experimental PXRD results were identical to the stimulated, **Figures 1c-d**, a hint that the synthesis approaches reached the targeted catalysts. Furthermore, the diffraction peak intensity of the 3D Sn-BDC is weaker than that of 2D Sn-BDC, revealing the low crystallinity of the sample prepared by the closed hydrothermal method. The experiments divulged a catalyst framework with 1, 4-benzene dicarboxylic acid (para-phthalic acid) as a linker and Sn nodes bound to O atoms in the as-synthesized Sn-BDC catalysts.

The surface morphology and micro-structures were detected using scanning electron microscopy (SEM) with respect to morphology and structure play a vital role in the physical and chemical properties of a catalyst that impact incredibly on performance. The SEM images, **Figures 1e-f**, reveal different topologies of well-shaped crystals with different sizes in all four Sn-MOF compounds from different organic linkers, reagents, reaction conditions and environments, that affected crystallization evidently unveiling different morphologies and topologies. It has been reported that Sn-MOF catalysts assume Sn (II) centres in tetra-coordinated settings, with the $5s^2$ lone pair inhabiting an edge of a distorted polyhedral framework. Hence, the polyhedral distortion indicates equivalence in the volume occupied by the Sn lone electron pairs while of oxide anion varies due to the nature of the organic linker and electron donor groups' motion[46].

Figure 1: Structures of (a) 1,4-Benzene Dicarboxylic Acid (BDC) Ligand, (b) Sn-BDC Catalyst (Sn, Green; C, Gray; O, Red), (c) PXRD Pattern of 2D Sn-BDC, (d) PXRD Pattern of 3D Sn-BDC, (e) SEM Images of 2D Sn-BDC, (f) SEM Images of 3D Sn-BDC.

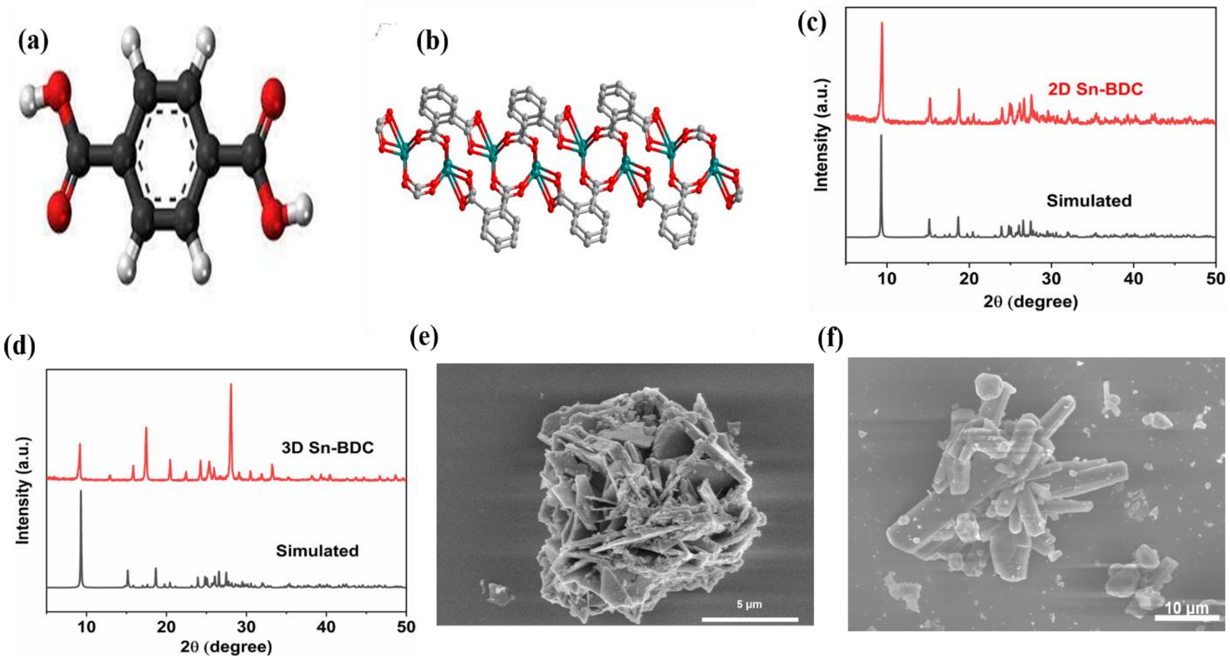

XPS survey tests were also executed on the 2D Sn-BDC and 3D Sn-BDC samples to discover the elemental composition. The XPS spectra of 2D Sn-BDC and 3D Sn-BDC are displayed in **Figures 2a-b**, respectively. In both spectra, the O 1s and C 1s are noticed at 532 eV and 285 eV, respectively. Moreover, for both samples, Sn peaks are also perceived in the spectra between 500 eV and 480 eV. Explicitly two discrete Sn 3d peaks are visible at 486.9 eV and 495.35 eV, **Figure 2c** attributed to the 3d $_{5/2}$ and 3d$_{3/2}$ states of Sn^{2+}. This testifies to the existence of Sn in the samples in the oxidation state of +2[45, 47]. Furthermore, two C 1s peaks are detected at 288.6 eV and 284.8 eV for C=C/C-C and O-C=O respectively, **Figure 2d**. Hence the observation of the peaks at 532 eV and 284.8 eV exhibits the availability of oxygen in the functionality of the synthesized Sn-BDC MOFs.

Figure 2: XPS Spectra of (a) 2D Sn-BDC, (b) 3D Sn-BDC, (c) 2D Sn-BDC Sn 3d, (d) 2D Sn-BDC C 1s Before Electrolysis.

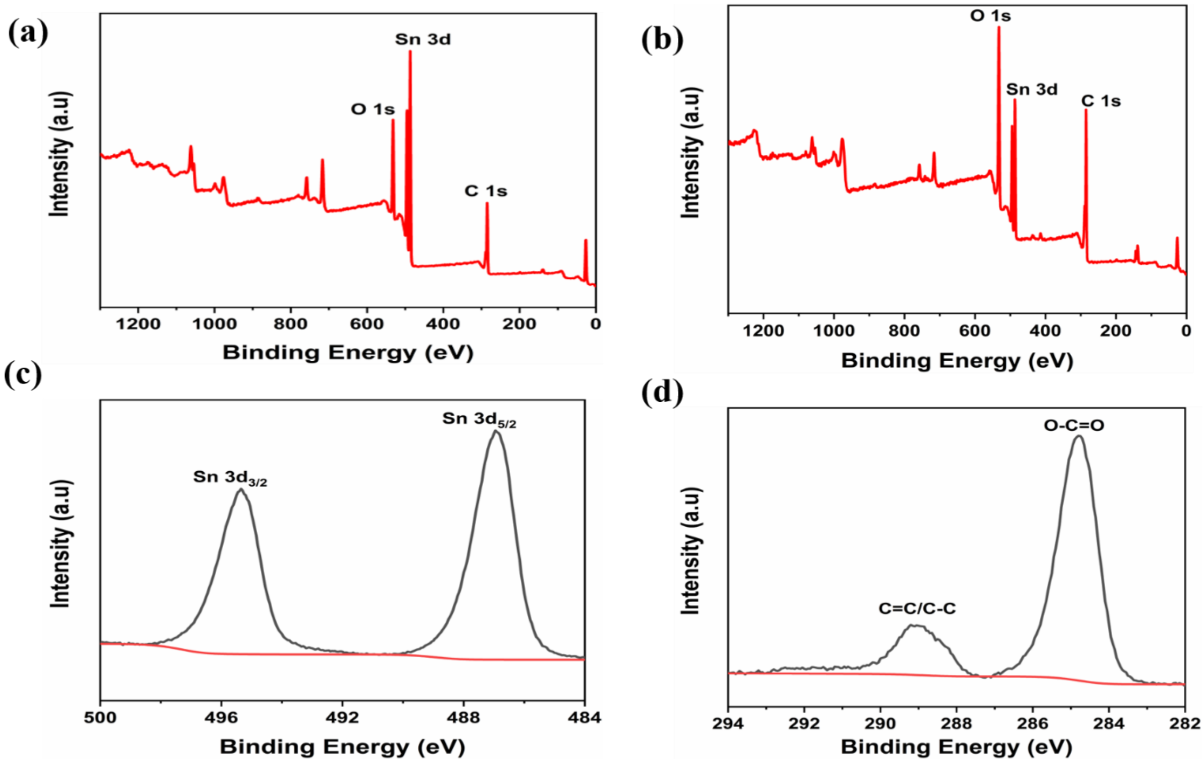

The qualitative and quantitative composition of the 2D Sn-BDC and 3D Sn-BDC samples were established by energy dispersive X-ray (EDX) spectroscopy [44]. The EDS mapping of micrometer-sized crystal particles confirms the presence and quantities of all the expected elements, (Sn, C, O) signifying that the targeted catalysts are successfully formed. The EDS of 2D Sn-BDC, and 3D Sn-BDC are presented in **Figures 3a-b** respectively. It was analyzed that 2D Sn-BDC possesses 7.2% weight of carbon with an atomic percentage of 20.5. Oxygen has a 28.2% weight and atomic percentage of 60.7 while tin was found to have a 64.6% weight and atomic percentage of 18.7. Similarly, 3D Sn-BDC consists of 55.6% weight of carbon with an atomic percentage of 37.9. Oxygen has a 40.6% weight and atomic percentage of 36.9 while tin was found to have a 3.7% weight and atomic percentage of 25.2.

The synthesis of Sn-BDC MOFs considers the formation of coordinated bonds between Sn ions and the BDC ligand that contribute to changes in spatial structure and symmetry of the organic ligand[48]. Hence, Fourier transform infrared (FTIR) spectroscopy was employed to confirm the successful synthesis of the targeted catalysts. As presented in **Figure 3c**, the FTIR spectra of 2D Sn-BDC and 3D Sn-BDC show some spectral mismatch with the BDC spectrum. Likewise, new peaks appear at 1691.3 – 1505.9 cm^{-1} and 1402.9 – 1316.4 cm^{-1}, which are accredited to the asymmetric stretching vibration ν_a(−COO-) and symmetric stretching vibration ν_s(−COO-) of the carboxylate ion[44, 48].

These changes confirm that Sn has successfully coordinated with the BDC ligand in producing the targeted catalysts. Also, the Sn-O peaks located at 532.6 cm^{-1} for the 2D Sn-BDC spectrum and at 558.3 cm^{-1} for the 3D Sn-BDC spectrum are stretching vibration characteristic peaks that confirm the existence of enough coordination of abundant carboxylate groups with tin ions.

Electron paramagnetic resonance (EPR) was employed to detect oxygen vacancies associated with either missing BDC linker defects or unsaturated Sn metal defects. The concentration of oxygen vacancies denotes the number of coordinatively unsaturated Sn metal atoms. This work managed to create defects in Sn-BDC samples through a change in the synthesis temperatures. **Figure 3d** shows that the 3D Sn-BDC synthesized at elevated temperatures in a closed hydrothermal approach has more defects than the 2D Sn-BDC MOF synthesized at mild temperatures in an open hydrothermal approach. The number of defects in MOFs can alter catalytic properties and performance through improvement in electronic structure and an increase in the catalyst's active sites[49]. However, the study has observed that an adequate number of defects is correlated with improved catalytic performance. Hence an excess number of defects may mean loss of structural integrity that might lead to loss of catalytic performance. Li and coworkers reported the highest conductivity and catalytic activity for ORR by β-MnO_2 with moderate oxygen defect concentration due to effective induced overlap of the surface d_{z2} orbitals that presented an extra donor level at the bottom of the conductive band[50]. Moreover, another work established that SnO_x with moderate content of oxygen defects was the most active surface that strongly suppressed hydrogen evolution reaction and possessed high HCOOH selectivity due to effective tuning of HCOO* adsorption strength[51].

Figure 3: (a) Energy Dispersive X-ray (EDX) Spectra of 2D Sn-BDC, (b) EDX Spectra of 3D Sn-BDC Catalysts, (c) Fourier Transform Infrared (FTIR) Spectrum of BDC, 2D Sn-BDC, and 3D Sn-BDC Samples, (d) Electron Paramagnetic Resonance (EPR) Spectra for 2D Sn-BDC and 3D Sn-BDC.

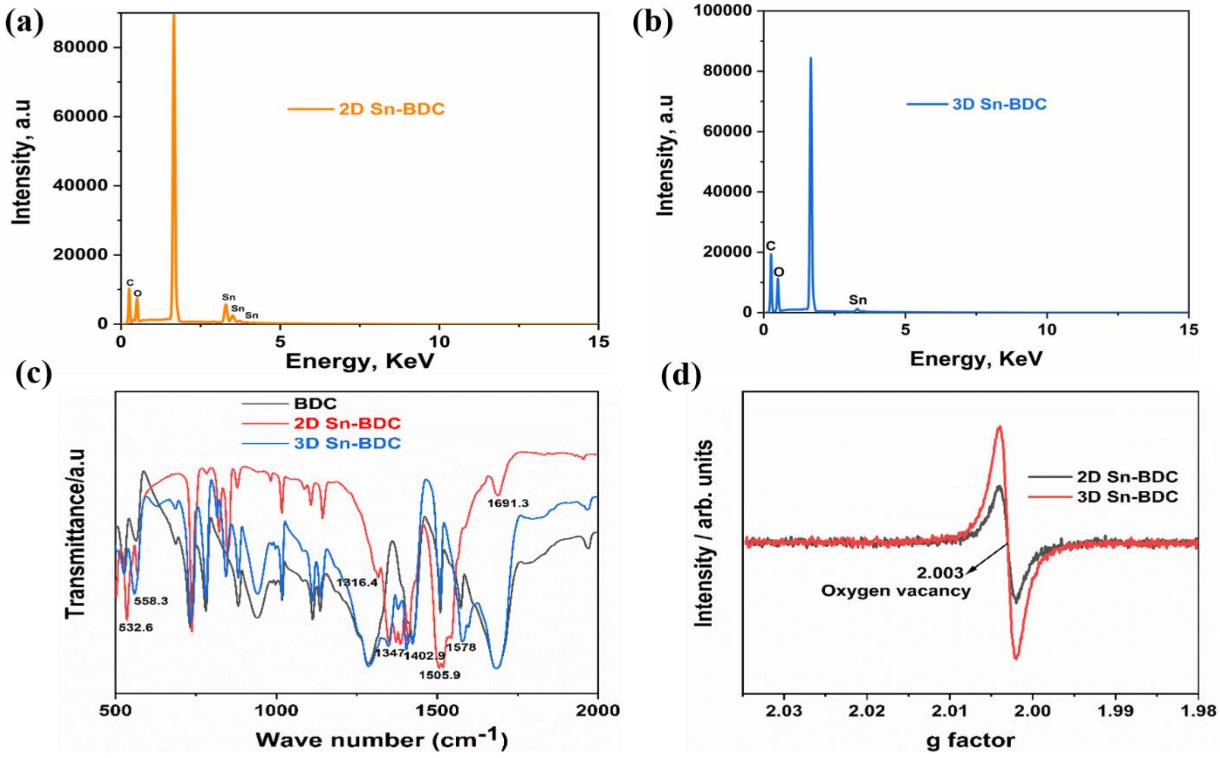

Electrochemical CO_2 Reduction Performance of 2D Sn-BDC and 3D Sn-BDC

In order to discover the activity of the catalysts for eCO_2RR, we studied the current-voltage curves for 2D Sn-BDC, and 3D Sn-BDC from cyclic voltammetry (CV) scans in CO_2-saturated 0.5 M $KHCO_3$ (pH = 7.34) and in N_2-saturated 0.5 M $KHCO_3$ (pH = 8.94) solution at a scan rate of 20 mV s^{-1}. **Figure 4a-b** portrays the CV curves in which at negative potentials, the sharp rise of the current densities can be perceived under both N_2 and CO_2. It was detected that with N_2, the rise is due to the reduction of H_2O from the hydrogen evolution reaction while under CO_2, the improved current is due to the reduction of both H_2O and CO_2. Accordingly, it was observed that in all the samples, the CO_2 current densities were higher than the N_2 current densities, signifying the dominance of the CO_2 reduction reaction (CO_2RR) over the hydrogen evolution reaction (HER). Furthermore, a large difference exists in the reduction of current densities under N_2 and under CO_2 for 2D Sn-BDC, which can be aligned to an improved CO_2RR and effective inhibition of HER. In contrast, there exists a smaller difference in the reduction current densities under N_2 and under CO_2 for 3D Sn-BDC a sign of an increased HER. Besides, it can be noticed that the reduction current density under N_2 for the 2D Sn-BDC electrode is evidently smaller than that of the 3D Sn-BDC sample, signifying the impact of morphology differences on the suppression of HER.

In order to further understand the improved performance of 3D Sn-BDC, compared to 3D Sn-BDC, electrolysis experiments were performed at potentials ranging from -0.57 V to -0.97V (vs. RHE), 0.1 V as the interval) to probe the effect of electrolysis potential on eCO_2RR. Similarly, the experiments showed the relationship between the electrolysis current density with electrolysis time at varied potentials. The study revealed an increase in electrolysis total current density from -0.57 to -0.97 V (vs. RHE) potentials of all the samples, **Figures 4c-d**. The current density remained constant in almost all the potentials within the experimental time, an indication of a good cathodic reaction, but slightly changed at -0.97 V (Vs. RHE) due to enhanced hydrogen evolution. The sample 2D Sn-BDC achieved a maximum current density of 37.4 mA cm^{-2} while 3D Sn-BDC had 20.6 mA cm^{-2} at -0.97 V (Vs. RHE) respectively. The exceptional performance could be aligned to an improved morphology with high active Sn centres for CO_2RR and a lower energy barrier in creating $^*OCHO$ intermediate from CO_2^- persuaded by Sn nodes which further eases the formation of $HCOO^-$[45, 52]

We further reliably used gas chromatography and high-performance liquid chromatography to determine and quantify the eCO_2RR products for the gaseous and liquid products respectively[4]. It was shown that 2D Sn-BDC had formate ($HCOO^-$) as a major CO_2 product with a very minimal amount of CO and H_2 compared to 3D Sn-BDC, **Figures 4e-f**. The 2D Sn-BDC displayed good eCO_2RR performance compared with the 3D Sn-BDC catalyst with FE_{max} ($_{HCOO^-}$) = 96.3%, j_{HCOO^-}, = 10.0 mA cm^{-2} and overpotential (η) = 0.42. In contrast, 3D Sn-BDC had a FE_{max} ($_{HCOO^-}$) = 88.7%, j_{HCOO}, = 8.5 mA cm^{-2} and overpotential (η) = 0.52. The faradaic efficiency of the CO_2 reduction to formate has a direct influence on the energy efficiency of the practice, higher faradic efficiency suggests a higher $HCOO^-$ rate and, subsequently, lower energy consumption[8]. The enriched activity and selectivity towards formate of 2D Sn-BDC nanosheets may be accredited to the improved morphology and number of active sites that aided mass and charge transfers.

Figure 4: Cyclic Voltammetry Scans in N_2- and CO_2-Saturated 0.5 M $KHCO_3$ for Catalysts: (a) 2D Sn-BDC, (b) 3D Sn-BDC; Total Current Densities in 0.5 M $KHCO_3$ CO_2-Saturated Electrolyte at Different Potentials as Indicated for (c) 2D Sn-BDC and (d) 3D Sn-BDC; Faradaic Efficiencies of H_2, CO, and HCOOH at Different Operation Voltages for Catalysts (e) 2D Sn-BDC and (f) 3D Sn-BDC in 0.5 M $KHCO_3$ CO_2-Saturated Electrolyte.

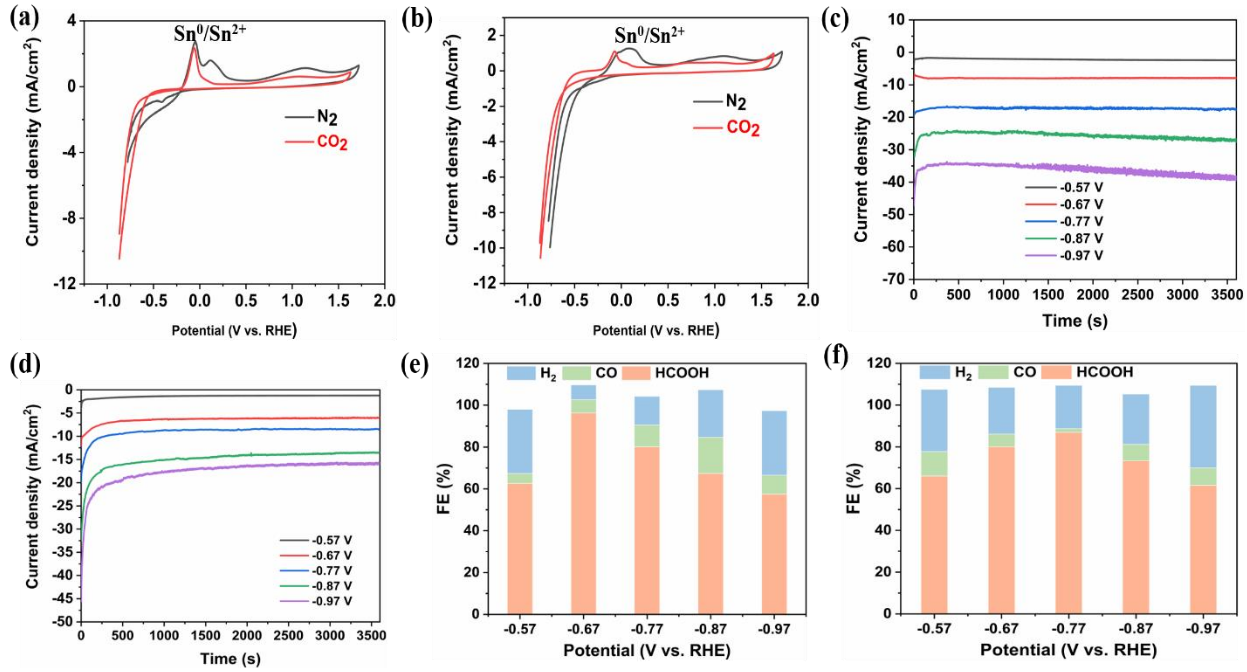

In addition, the stability of electrocatalysts is a major concern in eCO_2RR. The application of the as-synthesized Sn-BDC electrocatalysts for the eCO_2RR is further confirmed by assessing their stabilities. **Figures 5a-b**, show the stability evaluation at 2D Sn-BDC and 3D Sn-BDC electrodes and it was noticed that the stability of 2D Sn-BDC could be upheld for over 10 h, and its current density gradually changed from -8.5 mA cm^{-2} to -9 mA cm^{-2} at -0.67 V (Vs. RHE) and formate efficiency gradually changed from 96.29% to 86.03% within the 10 h of the experiment, **Figure 5a,** which probably came from the restructuring of the catalyst for the CO_2 reduction. Similarly, an over 10 h stability could be observed, **Figure 5b**, on 3D Sn-BDC with a current density change from -11 mA cm^{-2} to -12 mA cm^{-2} and FE change from 73.3% to 67.3% at -0. 87 V (Vs. RHE). The exceptional structure of the 2D Sn-BDC electrocatalyst may account for the good stability that was perceived. The improved morphology of Sn-MOFs retained the exposure of Sn^{2+} active sites and expedited the transport of electrolyte ions and CO_2 diffusion.

We further scrutinized catalyst electrodes before and after long electrolysis to get a perception of the structure of the active catalyst and the CO_2 reduction process. The crystal structure, morphological evolution and chemical composition of Sn-BDC MOFs after eCO_2RR were studied by PXRD and SEM. The PXRD patterns of the as-prepared samples confirmed that Sn-BDC was the only crystalline phase before eCO_2RR and SnO_2 was slowly generated at the expense of metallic Sn with the continuing CO_2 reduction. The SEM measurements revealed that after the electrochemical reaction, the 2D and 3D morphologies of the catalysts didn't collapse but possessed slight surface reconstruction, **Figure 5c-d**. Hence, the characterization results revealed slight instability of the Sn-BDC during a longer period of eCO_2RR.

Article DOI: https://doi.org/10.37284/ijpac.3.1.2738

To ascertain the effect of the transformed tin oxides in the eCO_2RR, we conducted the formate performance test on SnO_2 at potentials -0.57 V to -0.97 V (vs. RHE). SnO_2 achieved low current densities and FE_{HCOO^-} of 56.7%, and j_{HCOO^-} of 5.5 mA cm^{-2} at -0.87 V (V vs RHE). The results indicate low performance of SnO_2 compared to 2D Sn-BDC and 3D Sn-BDC at a wide range of potentials. This confirms the dominance of the synthesized Sn-BDC catalysts in the eCO_2RR into formate, regardless of the presence of the tin oxides. It testifies the relationship between the synthesis approach, structure and electrochemical performance of a catalyst in eCO_2RR.

Electrochemical impedance spectroscopy (EIS) is another advanced technique to study the activity of an electrode[45]. Here, the electrochemical impedance was analyzed by using the same three-electrode H-Type cell in 0.5 M $KHCO_3$ solution. The EIS gives knowledge about charge resistance transfer (Rct) which is a resistance at the electrolyte/ electrode boundary. This describes mass transport in reactions, conductivity and electrode's porosity. **Figure 5e** outlines EIS information of 2D Sn-BDC, 3D Sn-BDC and SnO_2. Besides, the Warburg diffusion coefficient (CPE) is related to charge transfer activity and its minimal value attests that a reaction proceeds through all diffusion-controlled phenomena. The EIS study discloses an R_{ct} of 42.98 Ω and CPE of 0.78975 Ω/s for 2D Sn-BDC. Likewise, 3D Sn-BDC yielded 60.12 Ω and 0.86261 Ω/s for R_{ct} and CPE respectively. In contrast, SnO_2 displayed R_{ct} of 148. 4 Ω and CPE of 0.91584 Ω/s.

Consistently, it was thrilling to realize that 2D Sn-BDC not only owned excellent activity, high selectivity and good stability but also displayed high turnover frequency (TOF). TOF was used to assess the real activity of effective active sites in the electrocatalysts. Consequently, the surface-active site density of electrochemically accessible 2D Sn-BDC was solved by integrating the Sn^0 / Sn^{2+} a CV anodic wave in an N_2-saturated electrolyte, that reached 8.809×10^{-8} mol cm^{-2}. Then, we found a TOF of the 2D Sn-BDC catalyst as high as 4887 h^{-1} at −0.97 V (vs. RHE), a sign of high utilization of surface-active sites. Similarly, the surface-active site density of electrochemically accessible Sn in 3D Sn-BDC was determined to be 9.767×10^{-8} mol cm^{-2}. Hence, the maximum TOF was calculated to be 2419 h^{-1} at −0.97 V (vs. RHE). This confirmed that the 2D Sn-BDC catalyst is an excellent electrocatalyst for high TOF performance in addition to other indicators of CO_2RR catalysis.

To elucidate the kinetics of the eCO_2RR, the Tafel study was performed on all the electrodes prepared from the two catalyst samples in a 0.5 M $KHCO_3$ electrolyte saturated with CO_2. The sample 2D Sn-BDC displayed a smaller Tafel slope of 218 mV dec^{-1} comparable to 3D Sn-BDC with a slope of 268 mV dec^{-1}, **Figure 5f**. In reference to the 118 mV dec^{-1} slope, it is established that all four samples had the first electron transfer as the rate-determining step for the eCO_2RR[53]. The smaller Tafel slope of 2D Sn-BDC signifies a much faster mass transport kinetics characteristic in comparison to other synthesized Sn-MOFs. Hence, we consider that a 2D Sn-BDC catalyst can enhance the *OCHO pathway and impede the *COOH pathway through Sn-O interaction, thus improving formate selectivity. It is reported that 2D MOFs have superior chemical and structural properties than 3D bulk MOFs due to ultrathin structure that promotes electrical conductivity, mass transport during reaction and enhanced electrocatalysis. Thus, the vacancies created in 2D compounds can boost the carrier concentration for enhanced electrical conductivity[54-56].

Figure 5: Stability Curves for 10 h Electrolysis Tests of Catalysts (a) 2D Sn-BDC and (b) 3D Sn-BDC in 0.5 M $KHCO_3$ CO_2-Saturated Electrolyte; SEM Images of Catalysts (c) 2D Sn-BDC and (d) 3D Sn-BDC After Electrolysis Tests; (e) Electrochemical Impedance Spectra of 2D Sn-BDC, 3D Sn-BDC, and SnO_2 in 0.5 M $KHCO_3$ Solution; (f) Tafel Slopes of 2D Sn-BDC (Black) and 3D Sn-BDC (Red).

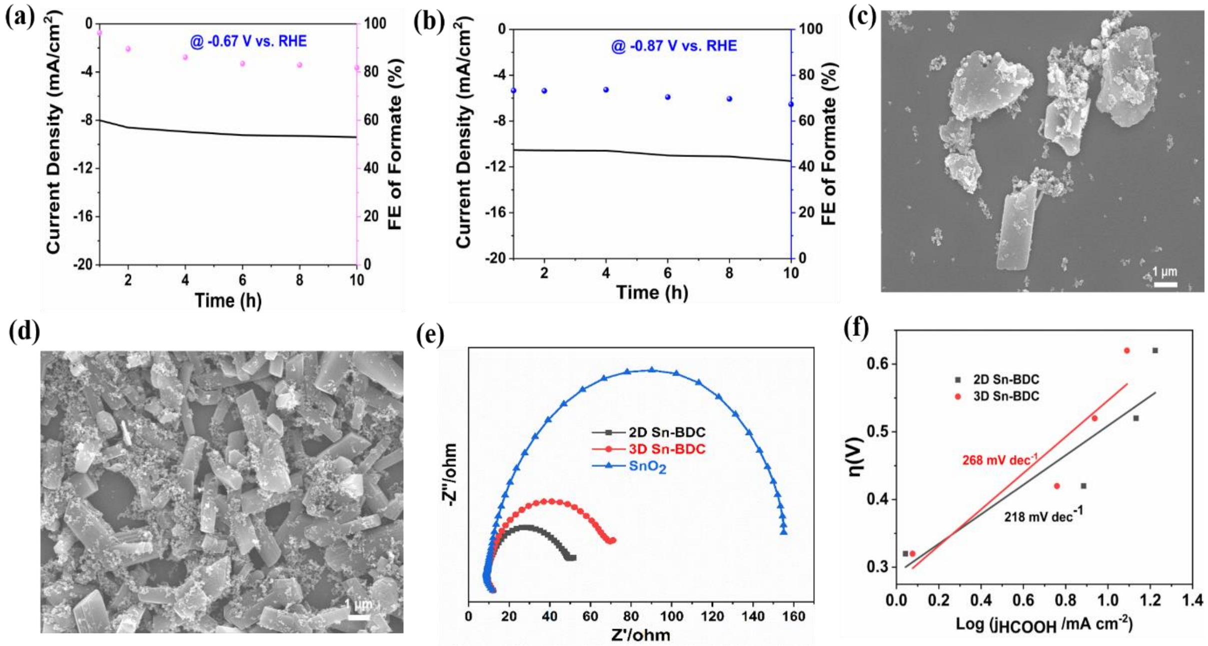

Comparison of 2D Sn-BDC in eCO_2RR Performance to Formate with Recent Reported Sn Catalysts

This work has established superior eCO_2RR of 2D Sn-BDC considered to originate from the ultrathin structure, improved surface area and surface vacancies. This performance is comparable to or higher than that of other related CO_2RR Sn-based electrocatalysts reported in very recent literature, **Table 1**. The comparison indicates the efficient CO_2RR kinetics catalyzed by the 2D Sn-BDC among the other Sn-based eCO_2RR.

Table 1: Electrochemical Reduction of Carbon Dioxide Performance by Tin-Based Catalysts.

Catalyst	$FE_{formate}$ (%)	Electrolyte	$J_{formate}$ ($mA\ cm^{-2}$)	Tafel slope ($mV\ dec^{-1}$)	η (V)	Ref.
2D Sn-BDC	96.3	0.5 M $KHCO_3$	10.0	167.0	0.42	This work
$Sn\text{-}MOF_{Pb5}$	94.6	0.5 M $KHCO_3$	25.0	138.2	0.85	[45]
Sn-MOF	91.8	0.5 M $KHCO_3$	23.2	173.0	0.95	[45]
V_0-SnO_2-60 min	92.4	0.5 M $KHCO_3$	18.8	76.0	0.45	[57]
Sn(101)/SnO_2/C	93.3	0.5 M $KHCO_3$	8.2	-	0.55	[42]
Sn-N6-MOF	85.0	0.5 M $KHCO_3$	23.0	-	0.98	[58]
$SnS_{0.55}$/CC	93.1	0.5 M $KHCO_3$	28.4	120.9	0.85	[52]
Sn/SnO_2@NC	83.0	0.5 M $KHCO_3$	17.0	-	0.65	[59]

SUMMARY

The performance of 2D Sn-BDC and 3D Sn-BDC catalysts for the transformation of CO_2 to formate synthesized through open and closed hydrothermal synthesis approaches are thoroughly investigated. The influence of the synthesis approach was observed in catalyst structure variations and CO_2 reduction performance differences of the as-synthesized catalysts. The 2D Sn-BDC displayed an improved performance compared with the other as-synthesized Sn-MOF catalysts for reduction of carbon dioxide with maximum FE_{HCOO^-} of 96.3%, j_{HCOO^-} of 10.0 mA cm^{-2} at overpotential (η) of 0.42, Tafel slope of 218 mV dec^{-1} and charge transfer resistance of 42.98 ohm arisen from enhanced morphology and more active sites that boosted the reduction process. In contrast, 3D Sn-BDC displayed maximum $FE(_{HCOO^-})$ of 88.7%, j_{HCOO^-}, of 8.5 mA cm^{-2} at overpotential (η) of 0.52, Tafel slope of 268 mV dec^{-1} and charge transfer resistance of 60.12 ohm. It is concluded that the 2D Sn-BDC catalyst is simple to prepare, cost-effective, environmentally friendly and prominent for large-scale application of eCO_2RR to formate.

Author Contributions

The manuscript was written through the contributions of all authors. All authors have given approval for the final version of the manuscript.

Acknowledgements

This work is supported by the National Natural Science Foundation of China (22174067, and 22204078), the Natural Science Foundation of Jiangsu Province of China (BK2019008 and BK20220370), Jiangsu Provincial Department of Education (22KJB150009), State Key Laboratory of Analytical Chemistry for Life Science (SKLACLS2218), the Priority Academic Program Development of Jiangsu Higher Education Institutions and Nalikule College of Education, Malawi.

Conflict of Interests

The authors declare no conflict of interest.

REFERENCES

[1] M. Aresta, A. Dibenedetto, A. Angelini, *Chem. Rev.* **2014**, *114*, 1709-1742.

[2] A. Rafiee, K. Rajab Khalilpour, D. Milani, M. Panahi, *J. Environ. Chem. Eng.* **2018**, *6*, 5771-5794.

[3] J. Wu, X.-D. Zhou, *Chinese J. Catal.* **2016**, *37*, 999-1015.

[4] S.-Z. Hou, X.-D. Zhang, W.-W. Yuan, Y.-X. Li, Z.-Y. Gu, *Inorg. Chem.* **2020**, *59*, 11298-11304.

[5] S. Y. Choi, S. K. Jeong, H. J. Kim, I.-H. Baek, K. T. Park, *ACS Sustain. Chem. Eng.* **2016**, *4*, 1311-1318.

[6] Y. Wang, J. Zhou, W. Lv, H. Fang, W. Wang, *Appl. Surf. Sci.* **2016**, *362*, 394-398.

[7] Z. Yang, F. E. Oropeza, K. H. L. Zhang, *APL Mater.* **2020**, *8*, 060901.

[8] N. Han, P. Ding, L. He, Y. Li, Y. Li, *Adv. Energy Mater.* **2020**, *10*, 1902338.

[9] S. C. Perry, P.-k. Leung, L. Wang, C. Ponce de León, *Curr Opin Electrochem* . **2020**, *20*, 88-98.

[10] Y. Ling, Q. Ma, Y. Yu, B. Zhang, *Transactions of Tianjin University* **2021**, *27*, 180-200.

[11] N. Kornienko, Y. Zhao, C. S. Kley, C. Zhu, D. Kim, S. Lin, C. J. Chang, O. M. Yaghi, P. Yang, *J. Am. Chem. Soc.* **2015**, *137*, 14129-14135.

[12] D. Narváez-Celada, A. S. Varela, *J. Mater. Chem. A* **2022**, *10*, 5899-5917.

[13] H.-L. Zhu, J.-R. Huang, P.-Q. Liao, X.-M. Chen, *ACS Central Science* **2022**, *8*, 1506-1517.

[14] Z. Di, Y. Qi, X. Yu, F. Hu, in *J. Catal. Vol. 12*, **2022**.

[15] P. S. Ho, K. C. Chong, S. O. Lai, S. S. Lee, W. J. Lau, S.-Y. Lu, B. S. Ooi, *Aerosol Air Qual. Res.* **2022**, *22*, 220235.

[16] J. D. Evans, B. Garai, H. Reinsch, W. Li, S. Dissegna, V. Bon, I. Senkovska, R. A. Fischer, S. Kaskel, C. Janiak, N. Stock, D. Volkmer, *Coordin. Chem. Rev.* **2019**, *380*, 378-418.

[17] Y. Yang, H. Dong, Y. Wang, C. He, Y. Wang, X. Zhang, *J. Solid State Chem.* **2018**, *258*, 582-587.

[18] T. Rasheed, K. Rizwan, M. Bilal, H. M. N. Iqbal, in *Molecules, Vol. 25*, **2020**.

[19] N. Aljammal, C. Jabbour, S. Chaemchuen, T. Juzsakova, F. Verpoort, in *J. Catal . Vol. 9*, **2019**.

[20] S. W. Jaros, M. F. C. Guedes da Silva, M. Florek, M. C. Oliveira, P. Smoleński, A. J. L. Pombeiro, A. M. Kirillov, *Crystal Growth Design* **2014**, *14*, 5408-5417.

[21] K. Wang, Z. Geng, M. Zheng, L. Ma, X. Ma, Z. Wang, *Crystal Growth Design* **2012**, *12*, 5606–5614.

[22] P. Manna, S. K. Das, *Crystal Growth Design* **2015**, *15*, 1407-1421.

[23] S. S. A. Shah, T. Najam, M. Wen, S.-Q. Zang, A. Waseem, H.-L. Jiang, *Small Structures* **2022**, *3*, 2100090.

[24] D. Kim, X. Liu, M. S. Lah, *Inorg. Chem. Frontiers* **2015**, *2*, 336-360.

[25] J. Gu, M. Wen, X. Liang, Z. Shi, M. V. Kirillova, A. M. Kirillov, *Crystals,* **2018**, 8.

[26] C. Pettinari, A. Tombesi, *MRS Energy Sustain.* **2020**, *7*, 35.

[27] Y. Zhang, X. Yang, H.-C. Zhou, *Polyhedron* **2018**, *154*, 189-201.

[28] P. C. Lemaire, D. T. Lee, J. Zhao, G. N. Parsons, *ACS Appl. Mater. Interfaces* **2017**, *9*, 22042-22054.

[29] P. Ji, K. Manna, Z. Lin, A. Urban, F. X. Greene, G. Lan, W. Lin, *J. Am. Chem. Soc.* **2016**, *138*, 12234-12242.

[30] L. J. Beeching, C. S. Hawes, D. R. Turner, S. R. Batten, *CrystEngComm* **2014**, *16*, 6459-6468.

[31] X. Wang, L. Liu, T. Makarenko, A. J. Jacobson, Crystal Growth & Design, **2010**, 10 (8).

[32] J. Wu, F. G. Risalvato, F.-S. Ke, P. J. Pellechia, X.-D. Zhou, *J. Electrochem. Soc.* **2012**, *159*, F353.

[33] A. Del Castillo, M. Alvarez-Guerra, J. Solla-Gullón, A. Sáez, V. Montiel, A. Irabien, *Appl. Energ.* **2015**, *157*, 165-173.

[34] W. Lv, R. Zhang, P. Gao, L. Lei, *J. Power Sources* **2014**, *253*, 276-281.

[35] S. Rasul, A. Pugnant, H. Xiang, J.-M. Fontmorin, E. H. Yu, *J. CO_2 Util.* **2019**, *32*, 1-10.

[36] S. Zhao, S. Li, T. Guo, S. Zhang, J. Wang, Y. Wu, Y. Chen, *Nano-Micro Letters* **2019**, *11*, 62.

[37] F. Cheng, X. Zhang, K. Mu, X. Ma, M. Jiao, Z. Wang, P. Limpachanangkul, B. Chalermsinsuwan, Y. Gao, Y. Li, Z. Chen, L. Liu, *Energy Technology* **2021**, *9*, 2000799.

[38] Y. F. Tay, Z. H. Tan, Y. Lum, *ChemNanoMat* **2021**, *7*, 380-391.

[39] W. J. Dong, C. J. Yoo, J.-L. Lee, *ACS Appl. Mater. Interfaces* **2017**, *9*, 43575-43582.

[40] X. Zheng, Y. Ji, J. Tang, J. Wang, B. Liu, H.-G. Steinrück, K. Lim, Y. Li, M. Toney, K. Chan, Y. Cui, *Nat. Catal.* **2019**, *2*.

[41] G. B. Damas, C. R. Miranda, R. Sgarbi, J. M. Portela, M. R. Camilo, F. H. B. Lima, C. M. Araujo, in *J. Catal . Vol. 9*, **2019**.

[42] J.-X. Wu, X.-R. Zhu, T. Liang, X.-D. Zhang, S.-Z. Hou, M. Xu, Y.-F. Li, Z.-Y. Gu, *Inorg. Chem.* **2021**, *60*, 9653-9659.

[43] Y. Peng, S. Sanati, A. Morsali, H. García, *Angew. Chem. Int. Ed.* **2023**, *62*, e202214707.

[44] Y. Wu, F. Li, Z. Lv, J. Xue, *ChemistrySelect* **2019**, *4*, 9403-9409.

[45] X. Wang, Y. Zou, Y. Zhang, B. Marchetti, Y. Liu, J. Yi, X.-D. Zhou, J. Zhang, *J. Colloid Interf. Sci* **2022**, *626*, 836-847.

[46] G. M. de Lima, R. I. Walton, G. J. Clarkson, R. S. Bitzer, J. D. Ardisson, *Dalton Trans.* **2018**, *47*, 8013-8022.

[47] S. Narayanaru, G. M. Anilkumar, M. Ito, T. Tamaki, T. Yamaguchi, *Catal. Sci. Technol.* **2021**, *11*, 143-151.

[48] B. J. Wang, S. Y. Ma, S. T. Pei, X. L. Xu, P. F. Cao, J. L. Zhang, R. Zhang, X. H. Xu, T. Han, *Sensors Actuators B: Chemical* **2020**, *321*, 128560.

[49] W. Xiang, Y. Zhang, Y. Chen, C.-j. Liu, X. Tu, *J. Mater. Chem. A* **2020**, *8*, 21526-21546.

[50] L. Li, X. Feng, Y. Nie, S. Chen, F. Shi, K. Xiong, W. Ding, X. Qi, J. Hu, Z. Wei, L.-J. Wan, M. Xia, *ACS Catal.* **2015**, *5*, 4825-4832.

[51] L. Li, Z.-J. Zhao, C. Hu, P. Yang, X. Yuan, Y. Wang, L. Zhang, L. Moskaleva, J. Gong, *ACS Energy Lett.* **2020**, *5*, 552-558.

[52] J. Liu, *Mater. Lab* **2022**, *1*.

[53] D. D. Zhu, J. L. Liu, S. Z. Qiao, *Adv. Mater.* **2016**, *28*, 3423-3452.

[54] K. Zhao, W. Zhu, S. Liu, X. Wei, G. Ye, Y. Su, Z. He, *Nanoscale Advances* **2020**, *2*, 536-562.

[55] T. Zhan, Y. Zou, Y. Yang, X. Ma, Z. Zhang, S. Xiang, *ChemCatChem* **2022**, *14*, e202101453.

[56] G. Zhan, H. C. Zeng, *Adv. Funct. Mater.* **2016**, *26*, 3268-3281.

[57] G. Liu, Z. Li, J. Shi, K. Sun, Y. Ji, Z. Wang, Y. Qiu, Y. Liu, Z. Wang, P. Hu, *Appl. Catalysis B: Environ.* **2020**, *260*, 118134.

[58] Y. Deng, S. Wang, Y. Huang, X. Li, *Chinese. J. Chem. Eng.* **2022**, *43*, 353-359.

[59] X. Teng, Y. Niu, S. Gong, X. Liu, Z. Chen. *J. Electrochem.* **2022**, *28*, 2108441.